Entanglement-assisted phase-estimation algorithm for calculating dynamical response functions

Rei Sakuma,[1,2] Shu Kanno,[2,3] Kenji Sugisaki,[2,4,5] Takashi Abe,[2] and Naoki Yamamoto[2,6]

[1]*Materials Informatics Initiative, RD Technology & Digital Transformation Center, JSR Corporation, 3-103-9 Tonomachi, Kawasaki-ku, Kawasaki 210-0821, Japan*

[2]*Quantum Computing Center, Keio University, 3-14-1 Hiyoshi, Kohoku-ku, Yokohama 223-8522, Japan*

[3]*Mitsubishi Chemical Corporation, Science & Innovation Center, Yokohama 227-8502, Japan*

[4]*Graduate School of Science and Technology, Keio University, 7-1 Shinkawasaki, Saiwai-ku, Kawasaki, Kanagawa 212-0032, Japan*

[5]*Centre for Quantum Engineering, Research and Education, TCG Centres for Research and Education in Science and Technology, Sector V, Salt Lake, Kolkata 700091, India*

[6]*Department of Applied Physics and Physico-Informatics, Keio University, 3-14-1 Hiyoshi, Kohoku-ku, Yokohama 223-8522, Japan*

(Received 11 May 2024; accepted 26 July 2024; published 23 August 2024)

Dynamical response functions are fundamental quantities to describe the excited-state properties in quantum many-body systems. Quantum algorithms have been proposed to evaluate these quantities by means of quantum phase estimation (QPE), where the energy spectra are directly extracted from the QPE measurement outcomes in the frequency domain. Accurate estimation of excitation energies and transition probabilities with these QPE-based approaches is, however, challenging because of the problem of spectral leakage (or peak broadening) which is inherent in the QPE algorithm. To overcome this issue, in this work we consider an extension of the QPE-based approach adopting the optimal entangled input states, which is known to achieve the Heisenberg-limited scaling for the estimation precision. We show that with this method the peaks in the calculated energy spectra are more localized than those calculated by the original QPE-based approaches, suggesting the mitigation of the spectral leakage problem. By analyzing the probability distribution with the entangled phase estimation, we propose a simple scheme to better estimate both the transition energies and the corresponding transition probabilities of the peaks of interest in the spectra. The validity of our prescription is demonstrated by numerical simulations in various quantum many-body problems: the spectral function of a simple electron-plasmon model in condensed-matter physics, the dipole transitions of the H_2O molecule in quantum chemistry, and the electromagnetic transitions of the ^{6}Li nucleus in nuclear physics.

DOI: 10.1103/PhysRevA.110.022618

I. INTRODUCTION

Studying the excited-state properties of many-body quantum systems are not only of academic interest but also crucial for industrial applications. Dynamical response functions and correlation functions are fundamental quantities that reflect the excited-state structures of a system and that describe responses of the system to an external field, which are directly connected to experimental results. The calculation of the response functions of many-body systems on a classical computer, however, remains a theoretical challenge as the computational cost scales exponentially with respect to the system size.

Quantum simulation of many-body systems is considered as a promising application for a quantum computer, and a number of papers have investigated how to compute the fermionic Green's function [1–17] as well as other dynamical response functions [16,18–24] efficiently on a quantum computer. A standard algorithm to compute response functions is to perform the real-time propagation of a given system on a quantum computer, followed by the Fourier transformation on a classical computer to calculate the energy spectra. This hybrid time-domain approach requires repeated measurements at each point on the time grid and sometimes is combined with further classical postprocessing, such as the convolution with some damping function [16] or interpolation or extrapolation of the results. These postprocessing operations make it difficult to extract from the calculated energy spectra the exact values of the transition energies and the corresponding transition probabilities, which are two important excited-state properties of the system.

Quantum phase estimation (QPE) [25,26] is one of the most fundamental quantum algorithms, and approaches have been proposed to use QPE in the calculation of dynamical response functions [4,17,19–21]. These methods may be considered as a time-domain approach that performs both the real-time propagation and the Fourier transformation on a quantum computer. The energy spectra are obtained directly by collecting the QPE measurement results in the frequency domain, and the resolution of the spectra can systematically be improved by increasing the number of qubits. These approaches, therefore, offer a promising way to calculate excited-state properties of a system on a quantum computer, combined with a number of ground-state preparation algorithms proposed [27–34].

Although the QPE-based approaches are attractive, QPE suffers a known problem of "spectral leakage" [35]; if the phase is not exactly on the QPE frequency grid, the measurement results "leak" from the exact position, resulting in a long tail in the measured probability distribution. This hinders the

accurate estimation of the transition energies and probabilities from the spectra calculated with the QPE-based approaches with a finite number of qubits. Several approaches have been proposed to address this leakage problem in the general context of QPE [35–37], but, to the best of our knowledge, no previous study has focused on the spectral properties of physical systems. Since peak broadening in calculations can be a major obstacle in making comparisons with experiments, addressing the leakage problem in the calculation of energy spectra is an urgent issue.

In this work, we consider mitigating this problem by employing entangled phase estimation (EPE), which performs QPE with the optimal entangled input state. Studies have shown [38–42] that with the optimal entangled input state the mean squared error (MSE) of the estimated phase scales as $O(N^{-2})$ with N the number of unitary operations for QPE, which is known as the Heisenberg limited scaling. We show that the probability distribution obtained with EPE has characteristics different from the original QPE-based one; most notably, the calculated spectra in EPE have much more localized peaks, thanks to the entangled input. Through the analysis of the EPE-based probability distribution, we propose a simple scheme to estimate the transition energies and corresponding transition probabilities of specified peaks in the spectra. We show that when this scheme is combined with the EPE-based calculation, the estimation error of the transition probabilities for isolated peaks is less than 1% in the limit of infinite sampling. This is a significant improvement over the original QPE-based calculation, whose worst-case error in the same setting is ≈10%. To demonstrate the usefulness of the proposed approach, we present numerical simulations of the spectral function of an electron-plasmon system, dipole transitions in quantum chemistry, and transition probabilities in nuclear physics.

II. METHOD

A. General formalism

We first outline the QPE-based approaches proposed in Refs. [4,17,19–21]. For a system described by the Hamiltonian H, our interest in this work is to calculate for a given operator B the following dynamical response function [20]:

$$S_B(\omega) = \sum_s |\langle\psi_s|B|\psi_0\rangle|^2 \delta(\omega - \Delta E_s), \tag{1}$$

where s label the eigenstates of the Hamiltonian with $s = 0$ corresponding to the ground state, $|\psi_s\rangle$ are the eigenstates with associated eigenenergies E_s, and $\Delta E_s = E_s - E_0$ are the transition energies. The prefactors or weights of the δ functions in Eq. (1), $|\langle\psi_s|B|\psi_0\rangle|^2$, are the transition probabilities. Equation (1) is related, via the Fourier transformation, to the Lehmann representation of the autocorrelation function $C_{BB}(t)$, where

$$C_{B_1B_2}(t) = \langle\psi_0|e^{iHt}B_1e^{-iHt}B_2|\psi_0\rangle \tag{2}$$

is the correlation function. We set $\hbar = 1$ throughout this work.

The general form of the quantum circuit used to evaluate Eq. (1) via QPE is shown in Fig. 1, which consists of three parts: The first register is for the QPE algorithm with n_q qubits, and $U_{in} = \mathrm{H}^{\otimes n_q}$ creates the unentangled input state of QPE with H the Hadamard gate. The second register is initialized to the ground state of the system $|\psi_0\rangle$ described with n_s qubits, and $U = \exp[i(H - E_0)T]$ is the time propagation operator. Here T is an artificial time introduced to scale the energy so that the energy range of interest becomes $[0, \frac{2\pi}{T}]$. The third (optional) register is an ancilla register with n_a qubits, which may be used to encode the B operator through the gate V_B. The measurement outcomes of the third register are used for postselection. As $B|\psi_0\rangle$ is expanded as $B|\psi_0\rangle = \sum_s \langle\psi_s|B|\psi_0\rangle|\psi_s\rangle$, the measurement results of the QPE register have a peak for each s near $\Delta E_s = E_s - E_0$ with the weight proportional to $|\langle\psi_s|B|\psi_0\rangle|^2$. More precisely, with a V_B-dependent normalization factor $\mathcal{N}$, the probabilities of measuring $k = 0, 1, 2, \ldots, 2^{n_q} - 1$ in the QPE register are given as

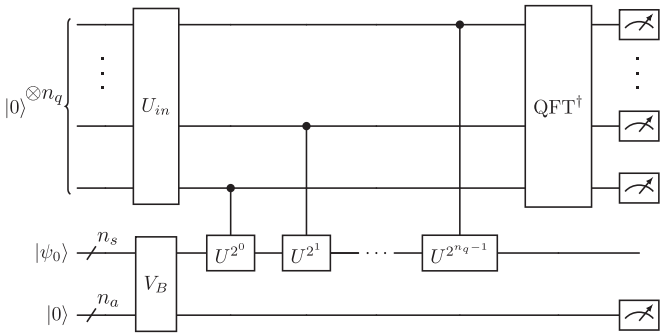

FIG. 1. The quantum circuit to evaluate $S_B(\omega)$ [$\bar{S}_B(\omega_k)$ in Eq. (7)]. Here $U = \exp[i(H - E_0)T]$ and QFT† represents the inverse quantum Fourier transform.

$$\mathcal{P}(k) = \mathcal{N} \sum_s |\langle\psi_s|B|\psi_0\rangle|^2 P(k|\Delta E_s T), \tag{3}$$

where

$$P(k|\theta) = \frac{1}{N_q}\left|\sum_{j=0}^{N_q-1} a_j e^{i\left(\theta - \frac{2\pi k}{N_q}\right)j}\right|^2 = \frac{1}{N_q^2}\frac{\sin^2\frac{\theta N_q}{2}}{\sin^2\frac{1}{2}\left(\theta - \frac{2\pi k}{N_q}\right)}, \tag{4}$$

$$a_j = \frac{1}{\sqrt{N_q}}. \tag{5}$$

Here $N_q = 2^{n_q}$ and a_j are the coefficients of the input state for QPE

$$\left|\phi_{in}^{\mathrm{QPE}}\right\rangle = \sum_{j=0}^{N_q-1} a_j|j\rangle, \tag{6}$$

created from $U_{in} = \mathrm{H}^{\otimes n_q}$ in Fig. 1. From $\mathcal{P}(k)$, an approximation of $S_B(\omega)$ is obtained as

$$\bar{S}_B(\omega_k) = \frac{1}{\mathcal{N}}\mathcal{P}(k), \tag{7}$$

where $\omega_k = \frac{2\pi}{N_q T}k$ are the frequency grid points in QPE.

In this approach one can also evaluate off-diagonal quantities, namely, the Lehmann representation of $C_{B_1B_2}(t)$ with $B_1 \neq B_2$, by considering $B_\pm = B_1 \pm B_2$ and $B_{i\pm} = B_1 \pm iB_2$. In the construction of the quantum circuit in Fig. 1 it is assumed that the ground state $|\psi_0\rangle$ and the ground-state energy E_0 are known *a priori*, and that one has access to controlled U gates. One possible way to avoid the dependencies on E_0 and controlled U gates using the concept of quantum phase difference estimation [43,44] is discussed in the Appendix.

One important application of this approach considered in Refs. [4,17] is the calculation of spectral function $A(\omega)$ in the electron many-body problem. This case corresponds to $B = c_\mu^\dagger$ and c_μ, which are the electron creation and annihilation operators for one-particle states μ, respectively. The spectral function of an N-electron system can be decomposed into the electron-creation (particle) part and the electron-annihilation (hole) part as

$$A(\omega) = \sum_\mu \left[A_\mu^{\text{particle}}(\omega) + A_\mu^{\text{hole}}(\omega)\right], \tag{8}$$

where

$$A_\mu^{\text{particle}}(\omega) = \sum_s |\langle\psi_{N+1,s}|c_\mu^\dagger|\psi_{N,0}\rangle|^2 \times \delta(\omega - (E_{N+1,s} - E_{N,0})), \tag{9}$$

$$A_\mu^{\text{hole}}(\omega) = \sum_{s'} |\langle\psi_{N-1,s'}|c_\mu|\psi_{N,0}\rangle|^2 \times \delta(\omega - (E_{N,0} - E_{N-1,s'})). \tag{10}$$

Here $|\psi_{N,0}\rangle$ is the ground state of the N-electron system with energy $E_{N,0}$, and $|\psi_{N\pm1,s}\rangle$ are the eigenstates of the $(N \pm 1)$-electron systems with corresponding eigenenergies $E_{N\pm1,s}$. The spectral function $A(\omega)$ is related to the diagonal elements of the retarded one-particle Green's function at zero temperature in the frequency domain [45] and can be compared with experimental spectra measured with photoemission and inverse photoemission spectroscopies. When the Jordan–Wigner transformation (JWT) is used, the V_B gate in Fig. 1 has a particularly simple form requiring only one ancilla qubit; in this case, c_μ and $c_\mu^\dagger$ are expanded with Pauli operators as

$$c_\mu = \left(\prod_{\nu<\mu} Z_\nu\right)\frac{X_\mu + iY_\mu}{2}, \tag{11}$$

$$c_\mu^\dagger = \left(\prod_{\nu<\mu} Z_\nu\right)\frac{X_\mu - iY_\mu}{2}, \tag{12}$$

and the V_B gate to calculate $A_\mu^{\text{particle}}(\omega)$ and $A_\mu^{\text{hole}}(\omega)$ is shown in Fig. 2. As the ancilla qubit at the bottom becomes 1 (0) when the μth orbital is occupied (unoccupied), by measuring this qubit as well as the QPE qubits both the particle and the hole parts of the spectral function can be sampled simultaneously. The true $A_\mu^{\text{particle}}(\omega)$ and $A_\mu^{\text{hole}}(\omega)$ should satisfy

$$\int_{-\infty}^{+\infty} \left[A_\mu^{\text{particle}}(\omega) + A_\mu^{\text{hole}}(\omega)\right]d\omega = 1, \tag{13}$$

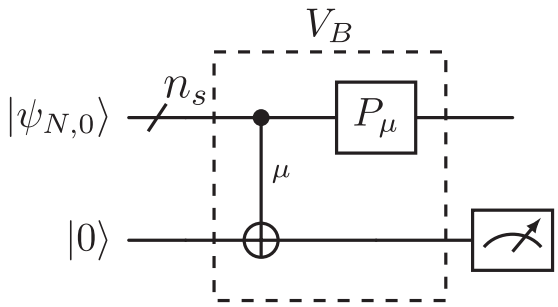

FIG. 2. The V_B gate in Fig. 1 for evaluating $A_\mu^{\text{particle}}(\omega)$ and $A_\mu^{\text{hole}}(\omega)$. Here $P_\mu = [\prod_{\nu<\mu} Z_\nu]X_\mu$ and the CNOT gate takes the μth qubit in $|\psi_{N,0}\rangle$ as control.

as can be verified by considering the anticommutation relation $c_\mu c_\mu^\dagger + c_\mu^\dagger c_\mu = 1$. This corresponds to setting $\mathcal{N} = 1$ in Eq. (7).

For a more general B, several approaches can be used to block encode B. The linear combination of unitary (LCU) approach [46] can be employed when B is represented as a sum of unitary operators as $B = \sum_{l=1}^{N_B} \lambda_l U_l$, where $\lambda_l \geqslant 0$ and U_l are unitary operators that act on the system qubits. In this case, V_B is expressed with $n_a = \lceil \log_2 N_B \rceil$ ancilla qubits as $V_B = \text{PREP}^\dagger \cdot \text{SELECT} \cdot \text{PREP}$, where

$$\text{PREP}|0\rangle^{\otimes n_a} = \frac{1}{\sqrt{\sum_l \lambda_l}} \sum_l \sqrt{\lambda_l}|l\rangle, \tag{14}$$

$$\text{SELECT} = \sum_l U_l \otimes |l\rangle\langle l|, \tag{15}$$

and $\bar{S}_B(\omega_k)$ is obtained by multiplying the probabilities of measuring $|k\rangle \otimes I^{\otimes n_s} \otimes |0\rangle^{\otimes n_a}$ states in Fig. 1 by $\left(\sum_l \lambda_l\right)^2$.

B. Use of entangled phase estimation

The spectra obtained in the QPE-based approaches, $\bar{S}_B(\omega_k)$, have nonzero values for all ω_k unless all $\Delta E_s T$ values are represented with n_q bits; this means that the peaks in $\bar{S}_B(\omega_k)$ can have long tails. This effect, called spectral leakage, can be mitigated by using entangled input states for QPE [38–42,47], where the coefficients a_j in Eqs. (5) and (6) are replaced by optimal ones. In this work, we focus on the following form:

$$a_j = \sqrt{\frac{2}{N_q}} \sin\frac{\pi j}{N_q}. \tag{16}$$

The corresponding U_{in} in Fig. 1 can be implemented by using the quantum Fourier transform gate [48] (or a shallower gate using ancilla qubits [42]), and with this form $P(k|\theta)$ in Eq. (3) becomes

$$P(k|\theta) = \frac{\cos^2\frac{\theta N_q}{2}}{2N_q^2} \frac{\sin^2\frac{\pi}{N_q}}{\sin^2\frac{\theta_{k+}}{2}\sin^2\frac{\theta_{k-}}{2}}, \tag{17}$$

where

$$\theta_{k\pm} = \theta - \frac{2\pi k}{N_q} \pm \frac{\pi}{N_q}. \tag{18}$$

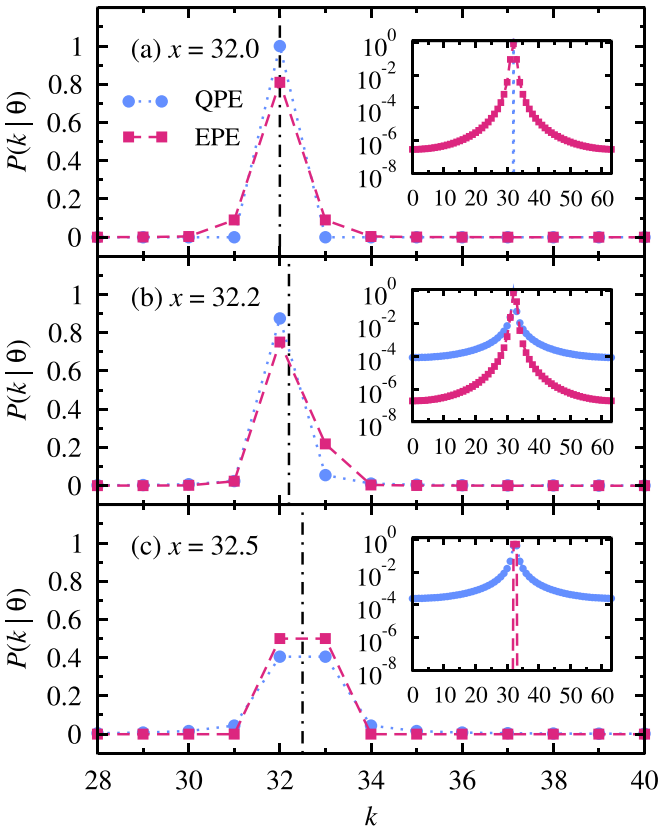

FIG. 3. Comparison of $P(k|\theta)$ in QPE and EPE for $n_q = 6$ ($N_q = 64$). The positions of θ are indicated by the vertical dash-dotted lines, and x is defined as $\theta = \frac{2\pi}{N_q}x$. (a) $x = 32.0$. (b) $x = 32.2$. (c) $x = 32.5$. The insets show $P(k|\theta)$ on a logarithmic scale.

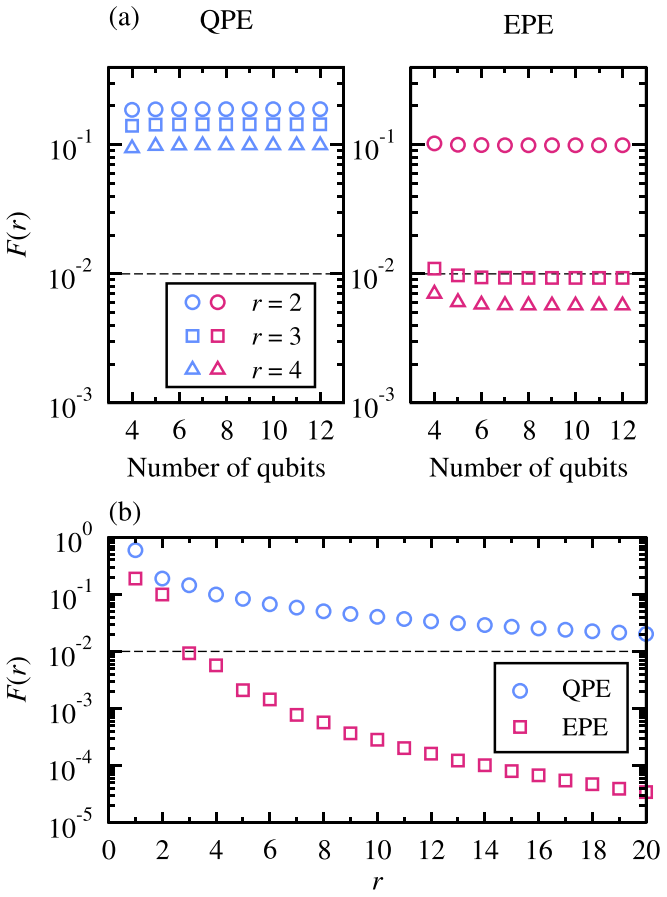

FIG. 4. (a) $F(r)$ in Eq. (21) as a function of n_q. (b) $F(r)$ as a function of r for $n_q = 12$ ($N_q = 4096$). The results with different value of n_q show a similar behavior.

Figure 3 compares $P(k|\theta)$ in QPE [Eq. (4)] and EPE [Eq. (17)] for three values of $\theta = \frac{2\pi}{N_q}x$. The most prominent feature of the EPE probability distribution is that, as can be seen in the inset of Fig. 3(b), the tail probability decreases more rapidly than the QPE one for general θ. It has been shown that, because of this property, the MSE of the estimated phase scales as $O(1/N_q^2)$ for large N_q [40,41]. As in the case of Fig. 3(a), when θ coincides with some $2\pi k_0/N_q$, where k_0 is an integer, in the original QPE algorithm $P(k|\theta)$ becomes δ_{k,k_0}, whereas in EPE $P(k = k_0|\theta) = 2(N_q^2 \tan^2 \frac{\pi}{2N_q})^{-1} < 1$. This means that, in EPE, when ΔE_s coincides with some $\omega_{k_0} = 2\pi k_0/T$, $\bar{S}_B(\omega_{k_0})$ is smaller than $|\langle\psi_s|B|\psi_0\rangle|^2$, and $\bar{S}_B(\omega_k)$ has nonzero tail probabilities. When θ is exactly at the midpoint of two grid points, as in Fig. 3(c), $P(k|\theta)$ in EPE takes nonzero values only at the two grid points, and this is another distinct feature of EPE.

C. Estimation of transition energies ΔE_s and the transition probabilities $|\langle\psi_s|B|\psi_0\rangle|^2$

First recall that, while the exact $S_B(\omega)$ in Eq. (1) consists of δ functions, $\bar{S}_B(\omega_k)$ in general has nonzero values for all ω_k. Consequently, the highest value in $\bar{S}_B(\omega_k)$ associated with a state s does not necessarily coincide with the true weight of the peak, $|\langle\psi_s|B|\psi_0\rangle|^2$. In the following, we consider a simple scheme to estimate ΔE_s and $|\langle\psi_s|B|\psi_0\rangle|^2$ for a specified peak.

Near $\omega_k \approx \Delta E_s$, the dominant contribution to $\bar{S}_B(\omega_k)$ comes from a single state s, therefore one may neglect the contributions from all $s' \neq s$ in Eq. (3). With this approximation, we propose the estimators for ΔE_s and $|\langle\psi_s|B|\psi_0\rangle|^2$ as

$$\Delta E_s^{\rm est} = \frac{\sum_k{}' \omega_k p_k}{\sum_k{}' p_k}, \tag{19}$$

$$|\langle\psi_s|B|\psi_0\rangle|^2_{\rm est} = \frac{1}{\mathcal{N}} \sum_k{}' p_k, \tag{20}$$

where the primes indicate that the sum is restricted to the points in the vicinity of the peak associated with the state s, and p_k are the probabilities of obtaining k in the measurement. In practice, for each s we calculate the sum in Eqs. (19) and (20) using the r highest-probability points near the observed peak, with r a positive integer. Note that here we do not take the maximum likelihood estimator for ΔE_s, i.e., the point ω_k corresponding to the highest probability. The reason for this is that, as can be seen in Fig. 3(b), even in ideal numerical simulations the maximum likelihood estimator has a bias from the true value of ΔE_s.

To find a reasonable value of r, in Fig. 4(a) we plot the following complementary cumulative probability

$$F(r) = \max_{\theta} \left[1 - \sum_{i=1}^{r} P(k_{p_i}|\theta) \right] \tag{21}$$

for $r = 2, 3, 4$ and $n_q = 4, \ldots, 12$, where $\{k_{p_i}\}$ are permutations of $\{k\}$ such that $P(k_{p_1}|\theta) \geqslant P(k_{p_2}|\theta) \geqslant \cdots$ for a given θ. This quantity serves as a measure of leakage in QPE and EPE and provides the confidence intervals of both approaches. In the QPE results [Fig. 4(a) left] with $r = 4$; for example, $F(r)$ is approximately 0.1 for all n_q, which indicates that for each peak approximately 10% of the measurement results will fall outside $r = 4$ highest-probability points in the worst case. This leakage can make accurate estimation in the original QPE-based approaches challenging. This issue becomes particularly problematic when the isolated-peak assumption is violated due to a high density of states, and the tails of other peaks overlap the peak of interest. It can be seen from Fig. 4(b) that simply increasing r is not an efficient solution to this problem because $F(r)$ in QPE decreases slowly with r. In contrast, the EPE results [Fig. 4(a) right] exhibit a different behavior; one can see that the results with $r = 3$ fall below 0.01 for $n_q > 4$, which means that, for each peak the measurement, results will fall into one of these three points with a probability of more than 99%. This indicates that, in EPE, for a single isolated peak well separated from others, the estimate of $|\langle\psi_s|B|\psi_0\rangle|^2$ via Eq. (20) with $r = 3$ approaches the true value within 1% of error as the number of samples increases, and this can be a useful criterion when analyzing the results. Also, Fig. 4(b) shows that the value of $F(r)$ for EPE decreases much faster than the case of QPE; this can be interpreted as the quadratically fast decrease of the variance of the peak or, in other words, the Heisenberg scaling of $F(r)$ with respect to r. Based on this analysis, in our numerical simulations presented in the next section we use $r = 3$. Choosing $r > 3$ improves the accuracy of the estimate in principle but may not be very practical because one needs a large number of samples to get statistically reliable results.

III. NUMERICAL SIMULATIONS

To get insights about the proposed approach, we perform numerical simulations of three simple systems. All our simulations are done with a noiseless state-vector-based simulator in the PennyLane library [49], therefore our results correspond to those in the limit of infinite sampling. The effect of finite sampling will be addressed in our future research. We employ the Trotter–Suzuki decomposition [50,51], but other approximate time-propagation approaches [52–56] can also be used.

A. Spectral function in the electron-plasmon model

Our first example is a simple system describing one electron and plasmons in a single mode, which is used to model core electron photoemission in metals [57–59]. The Hamiltonian is given as

$$H = \epsilon c^\dagger c + g c c^\dagger (b + b^\dagger) + \omega_p b^\dagger b, \tag{22}$$

where c and $c^\dagger$ are, respectively, creation and annihilation operators for the core electron of energy ϵ, $b^\dagger$ and b are bosonic operators for plasmons with energy ω_p, and g is the coupling coefficient. This model is exactly solvable [58], and the explicit form of the hole part of the spectral function $A^{\text{hole}}(\omega)$ [Eq. (10)] is given as

$$A^{\text{hole}}(\omega) = \sum_{n=0}^{\infty} \frac{1}{n!} e^{-(g/\omega_p)^2} \left(\frac{g}{\omega_p}\right)^{2n} \delta\left(\omega - \epsilon - \frac{g^2}{\omega_p} + n\omega_p\right). \tag{23}$$

Equation (23) consists of multiple plasmon excitations whose peak weights decrease exponentially with respect to plasmon number n. We calculate $A^{\text{hole}}(\omega)$ in this system using the proposed approach. The plasmons are treated using the method described in Ref. [60], which rewrites the bosonic part of the Hamiltonian to those of the harmonic oscillators. In the ground state of this system the core-electron level is fully occupied and no plasmon exists, therefore no ancilla qubit is needed. The plasmon wave function is expressed by the Gaussian function, which can be encoded with several approaches [61,62]. The parameters used in the simulation are $\epsilon = -1$, $\omega_p = 1$, $g = 0.8$, $n_s = 6$, and $T = 0.8$. The time propagation operator $\exp[i(H - E_0)T]$ is implemented with the first-order Trotter–Suzuki decomposition with the time step $\Delta T = 0.025$.

Figure 5(a) shows $A^{\text{hole}}(\omega)$ calculated with QPE and EPE for $n_q = 7$, together with the exact results from Eq. (23). In the plotted energy range there are four peaks whose heights decrease exponentially. The heights of EPE peaks are smaller than those in QPE, and, as expected, the tail of the EPE spectrum has a much smaller intensity, as can be seen in the inset of the figure. Figure 5(b) shows the estimated transition energy corresponding to the first (i.e., $n = 0$) peak via Eq. (19) calculated with QPE and EPE for $n_q = 6$–9. For comparison, the frequency grid points ω_k with the highest probability in the QPE and EPE spectra are also shown. It can be seen that, compared with the QPE estimates, which are more dependent on the values of the highest-probability frequency points, the EPE estimates are more robust and close to the exact result of $\epsilon + g^2/\omega_p = -0.36$ for all n_q. This result may be understood by noting that, as can be seen in Fig. 3(b), for general θ, the second largest probability value in the EPE probability distribution $P(k|\theta)$ is larger than its QPE counterpart.

Figure 5(c) shows the relative errors of the estimated weights (transition probabilities) of the first peak from the exact analytic result of $e^{-(g/\omega_p)^2} \approx 0.527$, obtained via Eq. (20) and also from the highest probability values extracted from the QPE and EPE spectra. Although the EPE peak heights (highest probability values) extracted from the spectra show large errors, as can also be seen in Fig. 5(a), EPE yields more accurate estimates than QPE. The relative errors in EPE are less than 0.01 for all n_q, which is consistent with our analysis for an isolated peak in the previous section. This result is reasonable because, as shown in the inset of Fig. 5(a), each of the EPE peaks has a very small overlap with neighboring peaks. The decrease in the EPE estimation error at $n_q = 9$ originates from the fact that the value of the exact transition energy in this case is positioned near the midpoint between two frequency grid points.

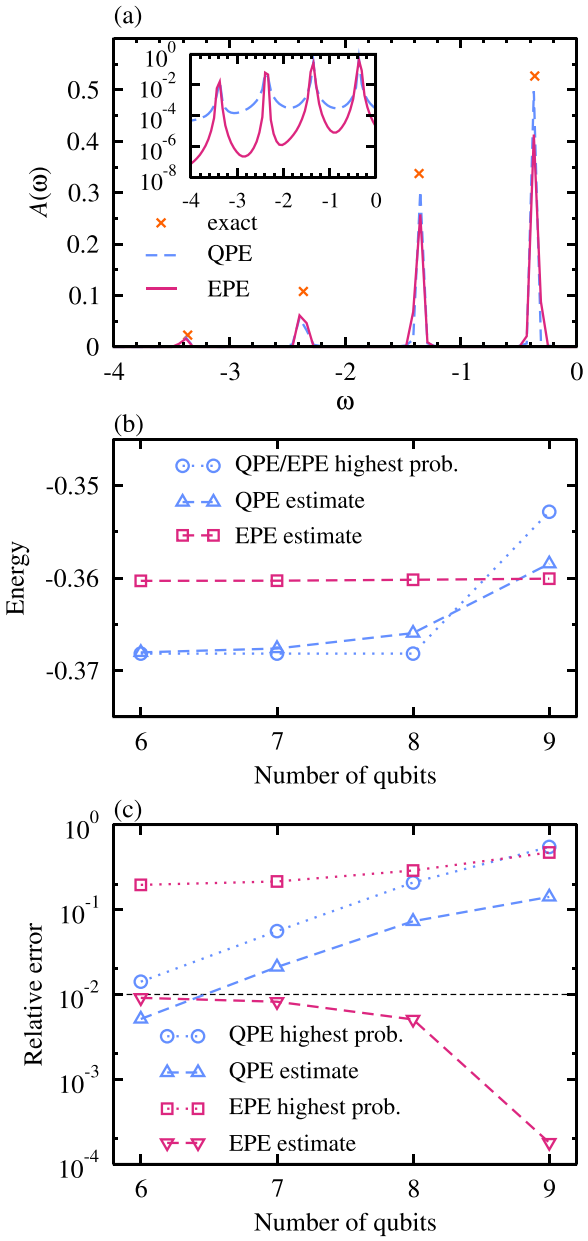

FIG. 5. (a) $A^{\text{hole}}(\omega)$ of the electron-plasmon system calculated with QPE and EPE for $n_q = 7$. The inset shows the same data on a logarithmic scale. (b) The estimates of the transition energy corresponding to the first peak for $n_q = 6$–9. (c) The relative estimation errors of the weight of the first peak for $n_q = 6$–9.

This situation is similar to the case in Fig. 3(c), where the estimation scheme in Eq. (20) becomes exact for $r \geqslant 2$ in EPE.

B. Dipole transitions of the H_2O molecule

Our next example is a quantum chemistry application of the current approach. We consider the dipole operators D^α as B in Eq. (1), where

$$D^\alpha = -\sum_{\mu\nu} d^\alpha_{\mu\nu}(c^\dagger_\mu c_\nu + c^\dagger_\nu c_\mu) + D^{c,\alpha} + D^{n,\alpha}. \tag{24}$$

Here $d^\alpha_{\mu\nu}$ are the dipole integrals defined as

$$d^\alpha_{\mu\nu} = \int \phi^*_\mu(\mathbf{r})\alpha\phi_\nu(\mathbf{r})d^3r, \tag{25}$$

where $\alpha = x, y, z$ are the position operators, ϕ_μ are the Hartree–Fock (HF) orbitals, and $D^{c,\alpha}, D^{n,\alpha}$ are the contributions from the core electrons and the nuclei, respectively. The quantity $S_{D^\alpha}(\omega)$ contains information about the transition dipole moments $|\langle\psi_s|D^\alpha|\psi_0\rangle|^2$ and the corresponding transition energies ΔE_s, from which the photoabsorption cross section and the oscillator strengths of a molecule can be calculated [63]. It is important to stress that in this approach no prior knowledge of the excited-state wave functions is required to calculate the excitation spectra. This is in contrast with approaches which calculate transition probabilities between some specific state pairs [64,65]. We consider the H_2O molecule with the orientation illustrated in Fig. 6(a). We use the STO-3G basis set and freeze the lowest two spatial HF orbitals. Therefore, our active space consists of five spatial HF orbitals (ten HF spin orbitals) and six electrons. We encode the system with the JWT, and employ the qubit tapering technique [66,67], using the particle-number conservation for spin-up and spin-down electrons. The number of qubits for the system after tapering is eight. The Hamiltonian matrix elements and the dipole integrals are taken from the PennyLane Quantum Chemistry Database [49]. The position operators in Eq. (24) are encoded with the LCU approach as explained in the method section. The number of Pauli operators are 19, 16, and 8 for $\alpha = x$, y, and z, respectively, requiring at most five ancilla qubits. The parameters for QPE are $T = 1.5$ a.u. and $n_q = 8$, and the second-order Trotter–Suzuki decomposition is used with the time step $\Delta T = 1.4/32 = 0.04375$.

Figures 6(b)–6(g) show $\bar{S}_{D^\alpha}(\omega_k)$ calculated with QPE and EPE and the estimates of the transition energies and the corresponding dipole moments using Eqs. (19) and (20). The exact spectra and the positions of all eigenstate levels (ΔE_s) are also indicated in the figures. The results using the HF ground state as $|\psi_0\rangle$ are also shown for comparison. It can be seen that only the $\alpha = x$ case [Figs. 6(b) and 6(c)] shows a nonzero peak at $\Delta E_s = 0$. This reflects the fact that the ground state of this molecule has a nonzero dipole moment element $\langle\psi_0|D^\alpha|\psi_0\rangle$ only for $\alpha = x$, when the orientation shown in Fig. 6(a) is used. This result suggests that, when $\langle\psi_0|B|\psi_0\rangle$ is known to have a nonzero value, as in the present case, one does not necessarily need to know the exact value of E_0 when constructing the quantum circuit in Fig. 1 but can extract it from the position of the first peak of the calculated spectra.

When the HF wave function is used as $|\psi_0\rangle$, the calculated peak heights change slightly, although their peak positions remain unchanged. This is because the HF wave function is written as a linear combination of eigenfunctions $|\psi_{\text{HF}}\rangle = \sum_u d_u|\psi_u\rangle$, and therefore $\mathcal{P}(k)$ given in Eq. (3) becomes $\mathcal{P}(k) = \mathcal{N}\sum_{s,u}|d_u|^2|\langle\psi_s|B|\psi_u\rangle|^2 P(k|\Delta E_s T)$. Note that in the current case the overlap between the exact and the HF wave functions is $|\langle\psi_{\text{HF}}|\psi_0\rangle|^2 \approx 0.9796$. Practically, since the HF ground state can easily be obtained and encoded, it may conveniently be used to get approximate energy spectra with a low computational cost, as long as

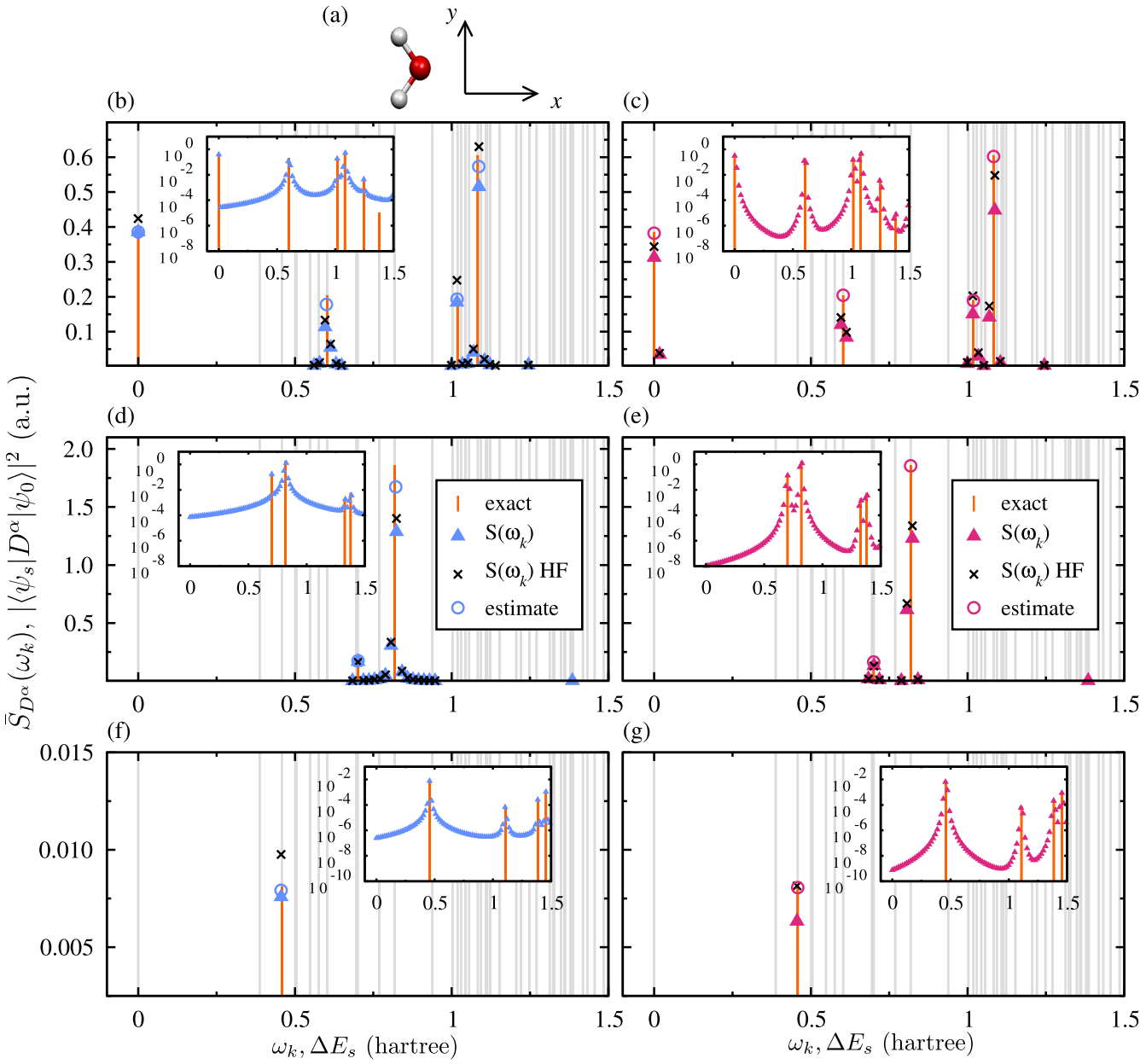

FIG. 6. (a) The orientation of the H_2O molecule in the simulation. (b)–(g) $\bar{S}_{D^\alpha}(\omega_k)$ and the estimates of ΔE_s and $|\langle\psi_s|D^\alpha|\psi_0\rangle|^2$ via Eqs. (19) and (20) for (b), (c) $\alpha = x$, (d), (e) y, and (f), (g) z calculated with (b), (d), (f) QPE and (c), (e), (g) EPE. The exact spectra and the positions of all eigenstate levels are indicated by the vertical orange (dark gray) and light gray bars, respectively. The insets show the results on a logarithmic scale.

the electron correlation in the system is not very strong. In the case where an accurate evaluation of the transition probability is desired, connecting sophisticated ground-state wave function preparation techniques to this approach is required.

As in the previous example, compared with the QPE results, the tail part of the EPE spectra decrease more rapidly, and the EPE peak heights are generally smaller. It can also be seen that the estimated $|\langle\psi_s|D^\alpha|\psi_0\rangle|^2$ in EPE are again in better agreement with the exact results. To see this quantitatively, in Table I we list the estimated values of ΔE_s and $|\langle\psi_s|D^\alpha|\psi_0\rangle|^2$ for selected transitions, together with the relative estimation errors of $|\langle\psi_s|D^\alpha|\psi_0\rangle|^2$. As for ΔE_s, both QPE and EPE estimates obtained via Eq. (19) are in good agreement with the exact results, but EPE slightly outperforms QPE. For $|\langle\psi_s|D^\alpha|\psi_0\rangle|^2$, the estimation errors of the EPE results are again less than 0.01 for all the cases. This indicates that the effects from the tails of other peaks are not very strong, therefore the approximation used in Eqs. (19) and (20) is valid. The accuracy of the QPE estimates of $|\langle\psi_s|D^\alpha|\psi_0\rangle|^2$ is, on the other hand, dependent on the values of ΔE_s. The QPE estimate for state s becomes accurate when the corresponding ΔE_s happens to be on or very close to some QPE frequency grid point ω_k. In our calculation the transition with $\Delta E_s = 0$ for $\alpha = x$ corresponds to this case, where the estimation error is 0.018%. The

TABLE I. The estimated values of ΔE_s and $|\langle\psi_s|D^\alpha|\psi_0\rangle|^2$ ($\alpha = x, y, z$), and the relative estimation errors of $|\langle\psi_s|D^\alpha|\psi_0\rangle|^2$ for selected transitions.

	ΔE_s (hartree)			$\lvert\langle\psi_s\rvert D^\alpha\lvert\psi_0\rangle\rvert^2$ (a.u.)			Relative error (%)	
α	Exact	QPE	EPE	Exact	QPE	EPE	QPE	EPE
x	0.000	0.000	0.000	0.386	0.386	0.382	0.018	0.933
	0.603	0.601	0.603	0.205	0.178	0.204	12.835	0.121
	1.019	1.017	1.019	0.190	0.193	0.189	1.700	0.577
	1.083	1.086	1.083	0.605	0.573	0.602	5.302	0.594
y	0.700	0.701	0.700	0.166	0.175	0.165	5.521	0.970
	0.818	0.822	0.818	1.860	1.673	1.854	10.025	0.311
z	0.458	0.456	0.458	0.008	0.008	0.008	2.487	0.795

corresponding EPE spectrum has a nonzero tail part, as can be seen in Fig. 6(c), which is consistent with the result in Fig. 3(a). For all other cases, EPE gives better agreement than QPE. This result suggests that QPE and EPE have complementary characteristics, and in practice it is possible to utilize both algorithms in order to derive accurate estimates.

C. Electromagnetic transitions of the ^{6}Li nucleus

Our final example is the shell-model calculation of electromagnetic transition probabilities in nuclear physics (see the textbooks, for example, Ref. [68]). We consider the transitions from the ground state to the excited states through the electric (E) and magnetic (M) multipole operators, which are denoted $\mathcal{M}_{\rm E}(l,m)$ and $\mathcal{M}_{\rm M}(l,m)$, respectively, with $l = 0, 1, 2, \ldots,$ the orbital angular momentum, and $m = -l, \ldots, +l$ its z component. Our interest here is to evaluate the reduced transition probability from the initial state (i) to the final state (f) defined as [68]

$$\mathcal{B}_{\rm E/M}(l; i \to f) = \sum_{m,M_f} \left|\left\langle I^{\pi_f}_{f,n_f} M_f \middle| \mathcal{M}_{\rm E/M}(l,m) \middle| I^{\pi_i}_{i,n_i} M_i \right\rangle\right|^2, \tag{26}$$

where the states are labeled by the total angular momentum I, the z component of the total angular momentum M, the parity π, and the additional quantum number to specify the states n. Because of the rotational symmetry, the states with the same I^π_n but with different M are degenerate. The reduced transition probabilities are related to the transition probabilities for emission and absorption of one photon through Fermi's golden rule [68]. The transition operators $\mathcal{M}_{\rm E/M}(l,m)$ and one-particle operators are written in the second quantization form as

$$\mathcal{M}_{\rm E/M}(l,m) = \sum_{\mu,\nu} \mathcal{M}_{\rm E/M}(l,m)_{\mu\nu} c^\dagger_\mu c_\nu. \tag{27}$$

From these operators we construct the following Hermitian operators:

$$\tilde{\mathcal{M}}_{\rm E/M}(l) = \sum_{\mu,\nu} \sum_{m=0}^{+l} \tilde{\mathcal{M}}_{\rm E/M}(l,m)_{\mu\nu} c^\dagger_\mu c_\nu, \tag{28}$$

where

$$\tilde{\mathcal{M}}_{\rm E/M}(l,m)_{\mu\nu} = \begin{cases} \mathcal{M}_{\rm E/M}(l,m)_{\mu\nu} & \text{for } m = 0 \\ \mathcal{M}_{\rm E/M}(l,m)_{\mu\nu} + (-1)^m \mathcal{M}_{\rm E/M}(l,-m)_{\mu\nu} & \text{for } m > 0, \end{cases} \tag{29}$$

and use them as the B operator in Eq. (1). The reduced transition probabilities $\mathcal{B}_{\rm E/M}(l; i \to f)$ and the corresponding transition energies $\Delta E_f = E_f - E_i$ are obtained from $\bar{S}_B(\omega_k)$ using our estimation scheme given in Eqs. (19) and (20). Here, we consider the ^{6}Li nucleus in the conventional nuclear shell model, which has one neutron and one proton in the valence space of the p shell consisting of 12 states (four for the neutron and proton $p_{1/2}$ orbitals and eight for the neutron and proton $p_{3/2}$ orbitals) on top of the ^{4}He closed core. We use the Cohen–Krath effective interaction [69] for the model space of the p shell. Recently, a benchmark study of the variational quantum eigensolver and the unitary coupled-cluster calculations was reported for this nucleus [70]. The initial state is taken to be the ground state of the system, $I^{\pi_i}_{i,n_i} = 1^+_1$ with $M_i = 0$. We note that the transitions between excited states are also of fundamental importance, and the current approach is applicable for these transitions in principle. As in the H_2O case above, we encode the system with the JWT and apply the qubit tapering technique [66,67] using the particle number conservation of neutrons and protons, which reduces the number of qubits in the system register from 12 to 10. We consider the electric quadrupole [$\mathcal{M}_{\rm E}(l=2)$] and the magnetic dipole [$\mathcal{M}_{\rm M}(l=1)$] transitions, which are denoted $E2$ and $M1$ transitions in short, respectively. The corresponding Hermitized transition operators, $\tilde{\mathcal{M}}_{\rm E}(l=2)$ and $\tilde{\mathcal{M}}_{\rm M}(l=1)$, are expanded with 56 and 74 Pauli operators, respectively. Instead of applying LCU to these operators directly, which would require six ancilla qubits in both cases, we diagonalize the one-particle matrix elements of $\tilde{\mathcal{M}}_{\rm E/M}(l)$ [Eq. (28)] and express the Hamiltonian and the Hermitized transition operators in terms of the eigenvectors of these matrices. Since $\tilde{\mathcal{M}}_{\rm E/M}(l)$ become diagonal in this basis, the number of Pauli operators is reduced to 12 in both cases, reducing the number of LCU ancilla qubits from six to four. The matrix elements of the nuclear Hamiltonian and transition operators are taken from the nuclear shell-model code KSHELL [71,72]. For the calculation of $E2$ transitions, the proton and neutron effective charges are

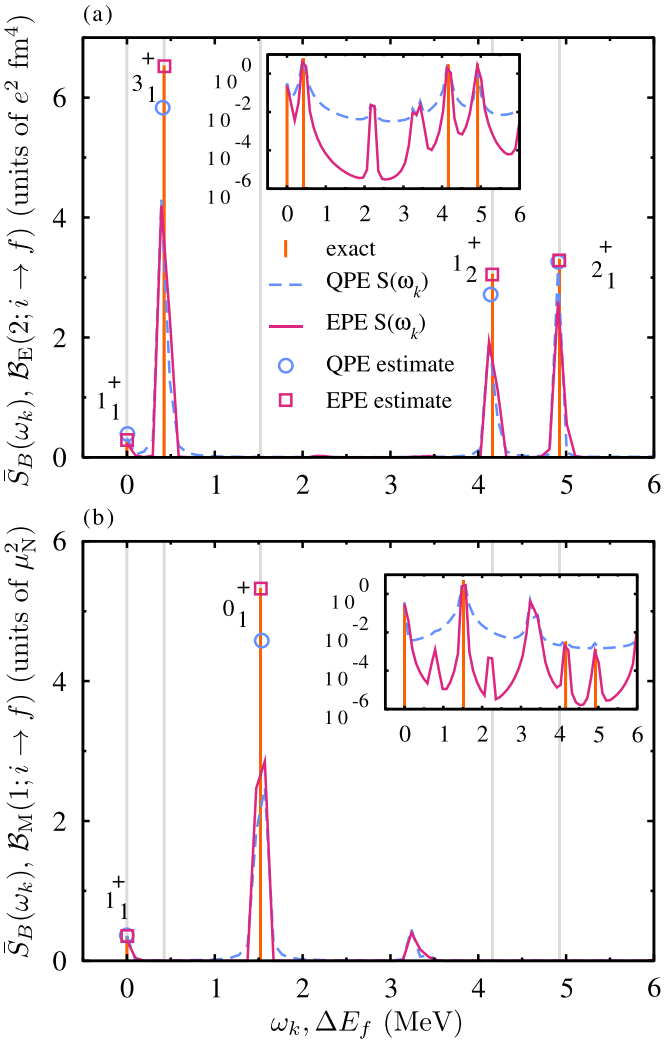

FIG. 7. $\bar{S}_B(\omega_k)$ and the estimates of ΔE_f and $\mathcal{B}_{\mathrm{E/M}}(l; i \to f)$ calculated with QPE and EPE for (a) $E2$ and (b) $M1$. The insets show $\bar{S}_B(\omega_k)$ on a logarithmic scale. The exact reduced transition probabilities and the positions of all eigenstate levels are indicated by the orange (dark gray) and light gray bars, respectively.

set to $1.5e$ and $0.5e$, respectively. For the calculation of $M1$ transitions, the gyromagnetic ratio of orbital angular momentum is taken as 1.0 (0.0) for the proton (neutron), and that of spin is taken as 5.585 (-3.826) for the proton (neutron). The parameters for QPE are $T = 1.0\ \mathrm{MeV}^{-1}$ and $n_q = 6$, and the second-order Trotter–Suzuki decomposition with the time step $\Delta T = 1.0/64\ \mathrm{MeV}^{-1} = 0.015\,625\ \mathrm{MeV}^{-1}$ is used.

Figures 7(a) and 7(b) show the calculated $\bar{S}_B(\omega_k)$ with QPE and EPE for $E2$ and $M1$ transitions. The estimates of ΔE_f and $\mathcal{B}_{\mathrm{E/M}}(l; i \to f)$ via Eqs. (19) and (20) are also shown together with the exact results. The estimated values and the relative estimation errors of $\mathcal{B}_{\mathrm{E/M}}(l; i \to f)$ are listed in Table II. Because of the limited energy resolution in the current calculation due to the small value of n_q, the calculated peaks are broader compared with the H_2O case above. However, one can still observe the same trend as those observed in the previous two systems; the peaks in the EPE results are again more localized, and the estimated values of ΔE_f and $\mathcal{B}_{\mathrm{E/M}}(l; i \to f)$ in EPE show a better agreement with the exact results. The relative estimation errors of $\mathcal{B}_{\mathrm{E/M}}(l; i \to f)$ in EPE are again less than 1% for most cases, as seen in Table II. The one exception is the result at $\Delta E_f = 0$ for $E2$, whose relative error is slightly above 1% (1.185%). This error comes from the tail of the neighboring large peak in $E2$ at $\Delta E_f \approx 0.424$ MeV corresponding to $1_1^+ \to 3_1^+$ transition, as seen in Fig. 7(a). This tail also significantly worsens the QPE estimate of the first peak, whose relative error is as large as ≈33%, showing a clear advantage of EPE. Unlike the H_2O case above, the QPE estimate of the first peak at $\Delta E_f = 0$ in the $M1$ transition [Fig. 7(b)] has a relatively large error of 2.769%. This is also because of the leakage effect from the neighboring large peak corresponding to $1_1^+ \to 0_1^+$ transition, even though these two peaks are separated by ≈1.523 MeV, corresponding to ≈16 QPE frequency grid points in the current calculation. Overall, the current results again demonstrate the effectiveness of the EPE-based approach, especially when the number of QPE qubits (n_q) is limited, or when the peaks in the spectra are closely located to each other.

Due to the high locality of the EPE probability distribution, in Figs. 7(a) and 7(b) one can also observe some low-intensity peaks only in the EPE results. In the QPE spectra, these low-intensity peaks are obscured by the tails of other peaks due to the spectral leakage problem. This enhanced peak-detection capability is another potentially useful feature of EPE.

We remark that some of the peaks in Figs. 7(a) and 7(b) correspond to transitions to high-lying excited states whose transition energies ΔE_f are outside the range of $[0, 2\pi/T]$.

TABLE II. The estimated values of ΔE_f and $\mathcal{B}_{\mathrm{E/M}}(l; i \to f)$, and the relative estimation errors of $\mathcal{B}_{\mathrm{E/M}}(l; i \to f)$. The transitions with $\Delta E_f = 0$ are related to the electric-quadrupole and magnetic-dipole moments of the ground state. The units of $\mathcal{B}_{\mathrm{E/M}}(l; i \to f)$ are $e^2\,\mathrm{fm}^4$ and μ_{N}^2 for $E2$ and $M1$ transitions, respectively.

		ΔE_f (MeV)			$\mathcal{B}_{\mathrm{E/M}}(l; i \to f)$			Relative error (%)	
Type	Transition	Exact	QPE	EPE	Exact	QPE	EPE	QPE	EPE
E2	$1_1^+ \to 1_1^+$	0.000	0.007	0.003	0.293	0.389	0.289	32.768	1.185
	$1_1^+ \to 3_1^+$	0.424	0.409	0.427	6.533	5.833	6.523	10.717	0.149
	$1_1^+ \to 1_2^+$	4.160	4.141	4.159	3.060	2.715	3.048	11.277	0.399
	$1_1^+ \to 2_1^+$	4.923	4.910	4.921	3.310	3.262	3.284	1.437	0.796
M1	$1_1^+ \to 1_1^+$	0.000	0.000	0.004	0.356	0.366	0.354	2.769	0.461
	$1_1^+ \to 0_1^+$	1.523	1.536	1.525	5.325	4.579	5.324	14.022	0.022

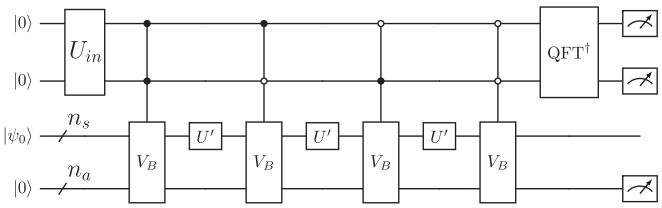

FIG. 8. A quantum circuit without depending on E_0 and controlled $\exp[iHT]$ for $n_q = 2$. Here $U' = \exp[iHT]$.

The most noticeable one is at around 3.2 MeV in Fig. 7(b). Practically, since the positions of these peaks depend on the value of T as $\omega = E_f - E_0 - \frac{2\pi}{T} m_f$ with m_f some positive integer, one can easily check if the observed peaks correspond to the transitions in the given energy range by varying T. For example, the peak at $\Delta E_f \approx 3.2$ MeV in Fig. 7(b) can be interpreted as the transition to the 2_3^+ state in comparison with the exact value $[\mathcal{B}_{\rm M}(1; 1_1^+ \to 2_3^+) \approx 0.562\ \mu_{\rm N}^2$ at $\Delta E_f \approx 9.550$ MeV].

IV. CONCLUSIONS AND OUTLOOK

In this work we have presented a quantum approach to calculate the spectral properties of many-body systems based on QPE with entangled input states and have shown that the calculated spectra have remarkable properties. The most notable feature is that the peaks in the calculated energy spectra are much more localized than those obtained with the original QPE-based approaches, thanks to the entanglement-assisted decrease of uncertainty of the peak width. Taking advantage of this property, we have proposed a simple scheme to estimate both the transition energy and the corresponding transition probability of selected states from the calculated spectra. For the latter quantity, we have shown that the estimation error in the proposed scheme is guaranteed to be less than 1% for isolated peaks in the limit of infinite sampling. Our proof-of-concept calculations show that the current approach is applicable to wide range of systems.

Since both the entangled input states considered in this study [Eq. (16)] and our estimation scheme can easily be implemented, they serve as a useful option for the QPE-based approaches. Other forms of the input states [73,74] as well as a more sophisticated estimation scheme should also be investigated.

Future work will focus on practical aspects of this approach. While our simulations are based on an ideal state-vector-based calculation with the exact ground state, in practice this approach requires accurate ground-state preparation and time-propagation schemes. In addition, as the number of samples (shots) available in real quantum devices is limited, it is important to develop techniques to sample only the most important energy region of the problem. Combining this approach with quantum amplitude amplification [75,76] or recently proposed efficient filtering approaches [77–79] could be an interesting research direction.

ACKNOWLEDGMENTS

R.S. is very grateful to Kaito Wada for technical discussions about optimal phase estimation and informing him of Ref. [41]. R.S. also would like to thank Hiroshi Yano, Kohei Oshio, and Mika Yoshimoto for helpful discussions. This work was supported by Quantum Leap Flagship Program (Grants No. JPMXS0118067285 and No. JPMXS0120319794) from the Ministry of Education, Culture, Sports, Science and Technology, Japan, and the Center of Innovations for Sustainable Quantum AI (JPMJPF2221) from Japan Science and Technology Agency. K.S. acknowledges support from KAKENHI Scientific Research C (21K03407) and Transformative Research Area B (23H03819) from Japan Society for the Promotion of Science. T.A. acknowledges support from KAKENHI Scientific Research C (21K03564).

APPENDIX: A WAY TO AVOID CONTROLLED $\exp[iHT]$ OPERATIONS AND DEPENDENCE ON E_0

The quantum circuit shown in Fig. 1 depends on the ground-state energy E_0 and controlled $U = \exp[i(H - E_0)T]$ operations. One possible way to remove these dependencies is to consider an operator whose action to a state $|j\rangle|\psi_0\rangle$ is given as (the ancilla register is omitted for simplicity)

$$\begin{aligned} |j\rangle|\psi_0\rangle &\to U'^j B U'^{N_q-1-j}|j\rangle|\psi_0\rangle \\ &= e^{iE_0T(N_q-1)} \\ &\quad \times \sum_s \langle\psi_s|B|\psi_0\rangle e^{i(E_s-E_0)Tj}|j\rangle|\psi_s\rangle, \end{aligned} \tag{A1}$$

where $U' = \exp[iHT]$ and $j = 0, 1, 2, \ldots, N_q - 1$. A quantum circuit implementing this idea is shown in Fig. 8 for $n_q = 2$. The controlled U operations are replaced with uncontrolled U' that do not depend on E_0, and instead one needs N_q multiply controlled V_B gates. This form can be advantageous when V_B has a relatively simple form, as in the case of Fig. 2.

[1] B. Bauer, D. Wecker, A. J. Millis, M. B. Hastings, and M. Troyer, Hybrid quantum-classical approach to correlated materials, Phys. Rev. X **6**, 031045 (2016).

[2] P.-L. Dallaire-Demers and F. K. Wilhelm, Method to efficiently simulate the thermodynamic properties of the Fermi-Hubbard model on a quantum computer, Phys. Rev. A **93**, 032303 (2016).

[3] S. Endo, I. Kurata, and Y. O. Nakagawa, Calculation of the Green's function on near-term quantum computers, Phys. Rev. Res. **2**, 033281 (2020).

[4] T. Kosugi and Y.-I. Matsushita, Construction of Green's functions on a quantum computer: Quasiparticle spectra of molecules, Phys. Rev. A **101**, 012330 (2020).

[5] Y. Tong, D. An, N. Wiebe, and L. Lin, Fast inversion, preconditioned quantum linear system solvers, fast Green's-function computation, and fast evaluation of matrix functions, Phys. Rev. A **104**, 032422 (2021).

[6] T. Keen, E. Dumitrescu, and Y. Wang, Quantum algorithms for ground-state preparation and Green's function calculation, arXiv:2112.05731.

[7] T. E. Baker, Lanczos recursion on a quantum computer for the Green's function and ground state, Phys. Rev. A **103**, 032404 (2021).

[8] F. Jamet, A. Agarwal, and I. Rungger, Quantum subspace expansion algorithm for Green's functions, arXiv:2205.00094.

[9] T. Keen, B. Peng, K. Kowalski, P. Lougovski, and S. Johnston, Hybrid quantum-classical approach for coupled-cluster Green's function theory, Quantum **6**, 675 (2022).

[10] J. Rizzo, F. Libbi, F. Tacchino, P. J. Ollitrault, N. Marzari, and I. Tavernelli, One-particle Green's functions from the quantum equation of motion algorithm, Phys. Rev. Res. **4**, 043011 (2022).

[11] F. Libbi, J. Rizzo, F. Tacchino, N. Marzari, and I. Tavernelli, Effective calculation of the Green's function in the time domain on near-term quantum processors, Phys. Rev. Res. **4**, 043038 (2022).

[12] N. Gomes, D. B. Williams-Young, and W. A. de Jong, Computing the many-body Green's function with adaptive variational quantum dynamics, J. Chem. Theory Comput. **19**, 3313 (2023).

[13] D. Cruz and D. Magano, Superresolution of Green's functions on noisy quantum computers, Phys. Rev. A **108**, 012618 (2023).

[14] A. Ralli, G. Greene-Diniz, D. M. Ramo, and N. Fitzpatrick, Calculating the single-particle many-body Green's functions via the quantum singular value transform algorithm, arXiv:2307.13583.

[15] G. Greene-Diniz, D. Z. Manrique, K. Yamamoto, E. Plekhanov, N. Fitzpatrick, M. Krompiec, R. Sakuma, and D. M. Ramo, Quantum computed Green's functions using a cumulant expansion of the Lanczos method, Quantum **8**, 1383 (2023).

[16] E. Kökcü, H. A. Labib, J. K. Freericks, and A. F. Kemper, A linear response framework for simulating bosonic and fermionic correlation functions illustrated on quantum computers, arXiv:2302.10219.

[17] K. Kowalski, N. P. Bauman, G. H. Low, M. Roetteler, J. J. Rehr, and F. D. Vila, Capturing many-body correlation effects with quantum and classical computing, arXiv:2402.11418.

[18] J. S. Pedernales, R. Di Candia, I. L. Egusquiza, J. Casanova, and E. Solano, Efficient quantum algorithm for computing n-time correlation functions, Phys. Rev. Lett. **113**, 020505 (2014).

[19] D. Wecker, M. B. Hastings, N. Wiebe, B. K. Clark, C. Nayak, and M. Troyer, Solving strongly correlated electron models on a quantum computer, Phys. Rev. A **92**, 062318 (2015).

[20] A. Roggero and J. Carlson, Dynamic linear response quantum algorithm, Phys. Rev. C **100**, 034610 (2019).

[21] T. Kosugi and Y.-I. Matsushita, Linear-response functions of molecules on a quantum computer: Charge and spin responses and optical absorption, Phys. Rev. Res. **2**, 033043 (2020).

[22] X. Cai, W.-H. Fang, H. Fan, and Z. Li, Quantum computation of molecular response properties, Phys. Rev. Res. **2**, 033324 (2020).

[23] W. J. Huggins, K. Wan, J. McClean, T. E. O'Brien, N. Wiebe, and R. Babbush, Nearly optimal quantum algorithm for estimating multiple expectation values, Phys. Rev. Lett. **129**, 240501 (2022).

[24] A. Kumar, A. Asthana, V. Abraham, T. D. Crawford, N. J. Mayhall, Y. Zhang, L. Cincio, S. Tretiak, and P. A. Dub, Quantum simulation of molecular response properties in the NISQ era, J. Chem. Theory Comput. **19**, 9136 (2023).

[25] A. Y. Kitaev, Quantum measurements and the Abelian stabilizer problem, arXiv:quant-ph/9511026.

[26] D. S. Abrams and S. Lloyd, Quantum algorithm providing exponential speed increase for finding eigenvalues and eigenvectors, Phys. Rev. Lett. **83**, 5162 (1999).

[27] A. Peruzzo, J. McClean, P. Shadbolt, M.-H. Yung, X.-Q. Zhou, P. J. Love, A. Aspuru-Guzik, and J. L. O'Brien, A variational eigenvalue solver on a photonic quantum processor, Nat. Commun. **5**, 4213 (2014).

[28] A. Anand, P. Schleich, S. Alperin-Lea, P. W. K. Jensen, S. Sim, M. Díaz-Tinoco, J. S. Kottmann, M. Degroote, A. F. Izmaylov, and A. Aspuru-Guzik, A quantum computing view on unitary coupled cluster theory, Chem. Soc. Rev. **51**, 1659 (2022).

[29] D. Poulin and P. Wocjan, Preparing ground states of quantum many-body systems on a quantum computer, Phys. Rev. Lett. **102**, 130503 (2009).

[30] Y. Ge, J. Tura, and J. I. Cirac, Faster ground state preparation and high-precision ground energy estimation with fewer qubits, J. Math. Phys. **60**, 022202 (2019).

[31] L. Lin and Y. Tong, Near-optimal ground state preparation, Quantum **4**, 372 (2020).

[32] Y. Dong, L. Lin, and Y. Tong, Ground-state preparation and energy estimation on early fault-tolerant quantum computers via quantum eigenvalue transformation of unitary matrices, PRX Quantum **3**, 040305 (2022).

[33] A. Kerzner, V. Gheorghiu, M. Mosca, T. Guilbaud, F. Carminati, F. Fracas, and L. Dellantonio, A square-root speedup for finding the smallest eigenvalue, Quantum Sci. Technol. **9**, 045025 (2024).

[34] Z. Ding, C.-F. Chen, and L. Lin, Single-ancilla ground state preparation via Lindbladians, Phys. Rev. Res. **6**, 033147 (2024).

[35] Y. Xiong, S. X. Ng, G.-L. Long, and L. Hanzo, Dual-frequency quantum phase estimation mitigates the spectral leakage of quantum algorithms, IEEE Signal Process. Lett. **29**, 1222 (2022).

[36] D. Nagaj, P. Wocjan, and Y. Zhang, Fast amplification of QMA, Quantum Inf. Comput. **9**, 1053 (2009).

[37] N. Wiebe and C. Granade, Efficient Bayesian phase estimation, Phys. Rev. Lett. **117**, 010503 (2016).

[38] A. Luis and J. Peřina, Optimum phase-shift estimation and the quantum description of the phase difference, Phys. Rev. A **54**, 4564 (1996).

[39] V. Bužek, R. Derka, and S. Massar, Optimal quantum clocks, Phys. Rev. Lett. **82**, 2207 (1999).

[40] W. van Dam, G. M. D'Ariano, A. Ekert, C. Macchiavello, and M. Mosca, Optimal quantum circuits for general phase estimation, Phys. Rev. Lett. **98**, 090501 (2007).

[41] Z. Ji, G. Wang, R. Duan, Y. Feng, and M. Ying, Parameter estimation of quantum channels, IEEE Trans. Inf. Theory **54**, 5172 (2008).

[42] R. Babbush, C. Gidney, D. W. Berry, N. Wiebe, J. McClean, A. Paler, A. Fowler, and H. Neven, Encoding electronic spectra in quantum circuits with linear T complexity, Phys. Rev. X **8**, 041015 (2018).

[43] K. Sugisaki, C. Sakai, K. Toyota, K. Sato, D. Shiomi, and T. Takui, Bayesian phase difference estimation: a general quantum algorithm for the direct calculation of energy gaps, Phys. Chem. Chem. Phys. **23**, 20152 (2021).

[44] K. Sugisaki, Projective measurement-based quantum phase difference estimation algorithm for the direct computation of eigenenergy differences on a quantum computer, J. Chem. Theory Comput. **19**, 7617 (2023).

[45] A. Fetter and J. Walecka, *Quantum Theory of Many-particle Systems*, Dover Books on Physics (Dover Publications, New York, 2003).

[46] A. M. Childs and N. Wiebe, Hamiltonian simulation using linear combinations of unitary operations, Quantum Inf. Comput. **12**, 901 (2012).

[47] P. Najafi, P. C. S. Costa, and D. W. Berry, Optimum phase estimation with two control qubits, AVS Quantum Sci. **5**, 023802 (2023).

[48] G. Rendon, T. Izubuchi, and Y. Kikuchi, Effects of cosine tapering window on quantum phase estimation, Phys. Rev. D **106**, 034503 (2022).

[49] V. Bergholm, J. Izaac, M. Schuld, C. Gogolin, S. Ahmed, V. Ajith, M. S. Alam, G. Alonso-Linaje, B. AkashNarayanan, A. Asadi, J. M. Arrazola, U. Azad, S. Banning, C. Blank, T. R. Bromley, B. A. Cordier, J. Ceroni, A. Delgado, O. D. Matteo, A. Dusko *et al.*, Pennylane: Automatic differentiation of hybrid quantum-classical computations, arXiv:1811.04968.

[50] H. F. Trotter, On the product of semi-groups of operators, Proc. Am. Math. Soc. **10**, 545 (1959).

[51] M. Suzuki, Generalized Trotter's formula and systematic approximants of exponential operators and inner derivations with applications to many-body problems, Commun. Math. Phys. **51**, 183 (1976).

[52] D. W. Berry, A. M. Childs, R. Cleve, R. Kothari, and R. D. Somma, Simulating Hamiltonian dynamics with a truncated Taylor series, Phys. Rev. Lett. **114**, 090502 (2015).

[53] D. W. Berry, A. M. Childs, and R. Kothari, Hamiltonian simulation with nearly optimal dependence on all parameters, in *2015 IEEE 56th Annual Symposium on Foundations of Computer Science, Berkeley, CA, USA* (IEEE, 2015), pp. 792–809.

[54] G. H. Low and I. L. Chuang, Optimal Hamiltonian simulation by quantum signal processing, Phys. Rev. Lett. **118**, 010501 (2017).

[55] G. H. Low and I. L. Chuang, Hamiltonian simulation by qubitization, Quantum **3**, 163 (2019).

[56] J. M. Martyn, Z. M. Rossi, A. K. Tan, and I. L. Chuang, Grand unification of quantum algorithms, PRX Quantum **2**, 040203 (2021).

[57] B. I. Lundqvist, Single-particle spectrum of the degenerate electron gas, Phys. Kondens. Mater. **6**, 193 (1967).

[58] D. C. Langreth, Singularities in the x-ray spectra of metals, Phys. Rev. B **1**, 471 (1970).

[59] L. Hedin, On correlation effects in electron spectroscopies and the *GW* approximation, J. Phys.: Condens. Matter **11**, R489 (1999).

[60] A. Macridin, P. Spentzouris, J. Amundson, and R. Harnik, Electron-phonon systems on a universal quantum computer, Phys. Rev. Lett. **121**, 110504 (2018).

[61] L. Grover and T. Rudolph, Creating superpositions that correspond to efficiently integrable probability distributions, arXiv:quant-ph/0208112.

[62] A. Kitaev and W. A. Webb, Wavefunction preparation and resampling using a quantum computer, arXiv:0801.0342.

[63] C. A. Ullrich, *Time-Dependent Density-Functional Theory: Concepts and Applications* (Oxford University Press, 2011).

[64] Y. Ibe, Y. O. Nakagawa, N. Earnest, T. Yamamoto, K. Mitarai, Q. Gao, and T. Kobayashi, Calculating transition amplitudes by variational quantum deflation, Phys. Rev. Res. **4**, 013173 (2022).

[65] N. P. Sawaya and J. Huh, Improved resource-tunable near-term quantum algorithms for transition probabilities, with applications in physics and variational quantum linear algebra, Adv. Quantum Technol. **6**, 2300042 (2023).

[66] S. Bravyi, J. M. Gambetta, A. Mezzacapo, and K. Temme, Tapering off qubits to simulate fermionic Hamiltonians, arXiv:1701.08213.

[67] K. Setia, R. Chen, J. E. Rice, A. Mezzacapo, M. Pistoia, and J. D. Whitfield, Reducing qubit requirements for quantum simulations using molecular point group symmetries, J. Chem. Theory Comput. **16**, 6091 (2020).

[68] A. Obertelli and H. Sagawa, *Modern Nuclear Physics* (Springer, 2021).

[69] S. Cohen and D. Kurath, Effective interactions for the 1p shell, Nucl. Phys. **73**, 1 (1965).

[70] O. Kiss, M. Grossi, P. Lougovski, F. Sanchez, S. Vallecorsa, and T. Papenbrock, Quantum computing of the ^{6}Li nucleus via ordered unitary coupled clusters, Phys. Rev. C **106**, 034325 (2022).

[71] N. Shimizu, T. Mizusaki, Y. Utsuno, and Y. Tsunoda, Thick-restart block Lanczos method for large-scale shell-model calculations, Comput. Phys. Commun. **244**, 372 (2019).

[72] N. Shimizu, Nuclear shell-model code for massive parallel computation, "KSHELL," arXiv:1310.5431.

[73] D. Patel, S. J. S. Tan, Y. Subasi, and A. T. Sornborger, Optimal coherent quantum phase estimation via tapering, arXiv:2403.18927.

[74] S. Greenaway, W. Pol, and S. Sim, A case study against QSVT: assessment of quantum phase estimation improved by signal processing techniques, arXiv:2404.01396.

[75] G. Brassard, P. Høyer, M. Mosca, and A. Tapp, Quantum amplitude amplification and estimation, in *Quantum Computation and Information Washington, DC, 2000*, Contemp. Math, Vol. 305 (Amer. Math. Soc., Providence, 2002), pp. 53–74.

[76] D. W. Berry, A. M. Childs, R. Cleve, R. Kothari, and R. D. Somma, Exponential improvement in precision for simulating sparse Hamiltonians, in *Proceedings of the Forty-Sixth Annual ACM Symposium on Theory of Computing*, STOC '14 (Association for Computing Machinery, New York, 2014), pp. 283–292.

[77] S. Lu, M. C. Bañuls, and J. I. Cirac, Algorithms for quantum simulation at finite energies, PRX Quantum **2**, 020321 (2021).

[78] M.-Q. He, D.-B. Zhang, and Z. D. Wang, Quantum Gaussian filter for exploring ground-state properties, Phys. Rev. A **106**, 032420 (2022).

[79] P. Zeng, J. Sun, and X. Yuan, Universal quantum algorithmic cooling on a quantum computer, arXiv:2109.15304.